B-Cu-Zn Gas Diffusion Electrodes for CO_2 Electroreduction to C_{2+} Products at High Current Densities

Yanfang Song, João R. C. Junqueira, Nivedita Sikdar, Denis Öhl, Stefan Dieckhöfer, Thomas Quast, Sabine Seisel, Justus Masa, Corina Andronescu, and Wolfgang Schuhmann*

Abstract: *Electroreduction of CO_2 to multi-carbon products has attracted considerable attention as it provides an avenue to high-density renewable energy storage. However, the selectivity and stability under high current densities are rarely reported. Herein, B-doped Cu (B-Cu) and B-Cu-Zn gas diffusion electrodes (GDE) were developed for highly selective and stable CO_2 conversion to C_{2+} products at industrially relevant current densities. The B-Cu GDE exhibited a high Faradaic efficiency of 79% for C_{2+} products formation at a current density of $-200\ mA\ cm^{-2}$ and a potential of $-0.45\ V$ vs. RHE. The long-term stability for C_{2+} formation was substantially improved by incorporating an optimal amount of Zn. Operando Raman spectra confirm the retained Cu^+ species under CO_2 reduction conditions and the lower overpotential for *OCO formation upon incorporation of Zn, which lead to the excellent conversion of CO_2 to C_{2+} products on B-Cu-Zn GDEs.*

Introduction

Worldwide climate change has become a regular topic in the news, as anthropogenic CO_2 levels have continued to steadily increase.[1–3] The direct conversion of CO_2 into chemical feedstocks or high energy-density fuels driven by renewable electricity is a potentially attractive technology to negate CO_2 emissions. However, despite many efforts being devoted to improving electrochemical CO_2 valorisation, development is still in the early-stages due to sub-optimal activity and product selectivity.[4–6] Employing gas diffusion electrode (GDE) systems has emerged as a promising approach to promote the electrochemical CO_2 reduction reaction (eCO2RR) towards possible applications.[3,7] By

overcoming the low solubility of CO_2 in aqueous electrolytes (approx. 35 mM) and shortening the diffusion path for the reaction, GDE-based systems can potentially reach industry-relevant current densities as opposed to the bathed electrodes utilized in a conventional H-cell.[7–9]

As catalyst for eCO2RR, Cu has been intensively studied due to its unique ability to produce hydrocarbons and alcohols, which is attributed to a moderate CO* binding energy.[10,11] The pre-oxidation of Cu has previously been reported to greatly improve the intrinsic catalytic properties towards C_{2+} products formation.[12] The catalytic role played by Cu^+ and subsurface oxygen was later revealed, where Cu^+ interacts synergistically with Cu^0 to promote C_{2+} products formation owing to the lower energy barrier for C–C coupling.[13–18] Despite some recent efforts on plasma-activated Cu,[16] electro-redeposited Cu,[17] and multi-hollow Cu_2O,[18] the stabilisation issue of Cu^+ under eCO2RR condition remains challenging.

Introducing modifier elements has been considered as an efficient strategy to reduce the tendency of Cu^+ reduction at negative potentials.[19–22] Boron has an electron configuration of $2s^2 2p^1$ and thus exhibits Lewis acidity. The empty electronic orbital of B tends to receive electrons from Cu, tuning the local electronic structure of Cu with positive valence sites and making it more Lewis acidic, both of which are favourable for boosting the formation of C_{2+} products in eCO2RR. A B-doped oxide-derived-Cu catalyst exhibited a higher Faradaic efficiency (FE) of 48.2% toward the formation of C_{2+} products than that of its boron-free oxide-derived-Cu counterpart (30.5%), owing to stabilisation of the Cu^+ species by the introduction of B.[21] By doping different amounts of B, the valence state of Cu could be tuned to achieve optimum C_{2+}

[*] Dr. Y. Song, J. R. C. Junqueira, Dr. N. Sikdar, Dr. D. Öhl, S. Dieckhöfer,
    T. Quast, Dr. S. Seisel, Prof. W. Schuhmann
    Analytical Chemistry-Center for Electrochemical Sciences (CES)
    Faculty of Chemistry and Biochemistry
    Ruhr University Bochum
    Universitätsstrasse 150, 44780 Bochum (Germany)
    E-mail: wolfgang.schuhmann@rub.de

    Dr. Y. Song
    CAS Key Laboratory of Low-Carbon Conversion Science and Engi-
    neering
    Shanghai Advanced Research Institute
    Chinese Academy of Sciences
    99 Haike Road, Shanghai 201203 (P. R. China)

    Dr. J. Masa
    Max Planck Institute for Chemical Energy Conversion
    Stiftstrasse 34–36, 45470 Mülheim an der Ruhr (Germany)

    Prof. C. Andronescu
    Chemical Technology III, Faculty of Chemistry and CENIDE
    Center for Nanointegration University Duisburg Essen
    Carl-Benz-Strasse 199, 47057 Duisburg (Germany)

    📃 Supporting information and the ORCID identification number(s) for
    ⃝iD the author(s) of this article can be found under:
   https://doi.org/10.1002/anie.202016898.

products formation with a high FE of 79% at −1.1 V vs. RHE in 0.1 M KCl.[22] However, the current densities in these reports (≤ 70 mA cm^{-2}) are far below any possible application.

In addition to a high FE towards particular desirable products and high current density, stable long-term operation is also highly important for viable application of a given catalyst for eCO$_2$RR.[23,24] In addition to the challenge of inherent chemical instability of Cu-based catalysts, catalyst degradation and cathodic corrosion under high cathodic potentials are similarly severe drawbacks.[7,23–27] Inhibition of these processes to stabilize Cu-based catalysts is important yet still challenging for the development of efficient eCO$_2$RR systems.

Herein, we report a B-doped Cu (B-Cu) catalyst for efficient eCO$_2$RR at industry-relevant current densities using a GDE electrolysis system. During operation especially at high current densities, GDEs are suffering from flooding due to electrowetting. Notably, this flooding problem, which characteristically leads to a low concentration of CO$_2$ at the triple-phase boundary due to low CO$_2$ solubility, was mitigated by controlling the amount of the hydrophobic binder PTFE (polytetrafluoroethylene) during catalyst ink preparation and the gas-liquid-catalyst interphase was further optimized by tuning the catalyst loading. As a result, a highest FE of 78% for C$_{2+}$ products formation (C$_2$H$_4$ 49%, C$_2$H$_5$OH 22%, C$_3$H$_7$OH 7%) was achieved on B-Cu GDE with 10% of PTFE and 0.5 mg cm^{-2} catalyst loading at −200 mA cm^{-2} and −0.45 V vs. RHE. Furthermore, a sacrificial anode of Zn, a less noble metal, was employed to stabilize B-Cu catalyst during eCO$_2$RR. With an optimum amount of incorporated Zn nanosheets (0.025 mg cm^{-2}), the long-term stability for C$_{2+}$ product formation at −200 mA cm^{-2} was significantly improved with an overall C$_{2+}$ product current density of −194 mA cm^{-2}. Operando electrochemical Raman spectroscopy (OERS) results show that the active Cu$^+$ species is stable even at high reduction potentials, the overpotential for *OCO formation is positively shifted by incorporation of Zn nanosheets, both of which contribute to the excellent eCO$_2$RR performance of B-Cu-Zn GDE.

Results and Discussion

The B-Cu catalyst was synthesized by a facile and scalable method[22,28,29] using concentrated sodium borohydride (NaBH$_4$) as both the reducing agent and boron source under continuous Ar purging. Zn nanosheets were synthesized by electrochemical deposition of Zn on a Cu foil followed by scratching them off. Figure 1 A displays the X-ray diffraction (XRD) pattern of the as-synthesized B-Cu sample. The main peaks at 2θ values of 43.3°, 50.4°, and 74.1° are corresponding to the (111), (200) and (220) planes, respectively, of cubic metallic Cu with a space group of $Fm\bar{3}m$ (COD: 9013014). In addition, weak peaks of cubic Cu$_2$O (111), (200), and (220) planes with a space group of $Pn\bar{3}m$ (COD: 1000063) are observed due to oxidation in air or Cu-B interaction with the solvent during synthesis. Similarly, peaks assigned to hexagonal Zn ($P6_3/mmc$, COD: 9012435) and ZnO ($P6_3mc$, COD:
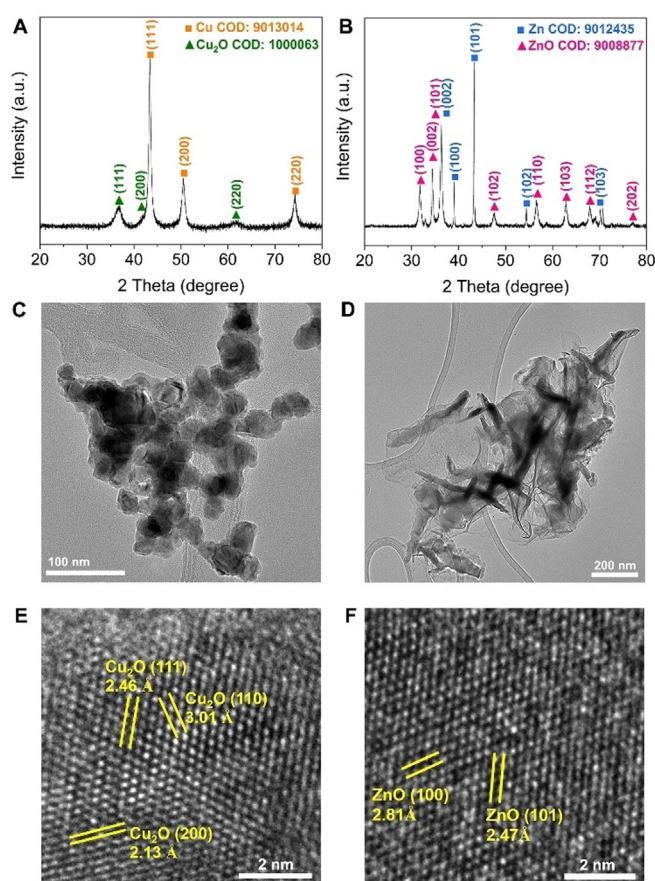
Figure 1. XRD patterns of A) B-Cu nanoparticles and B) Zn nanosheets. TEM images of C) B-Cu nanoparticles and D) Zn nanosheets. HRTEM images of E) B-Cu nanoparticles and F) Zn nanosheets.

9008877) are both observed in the XRD pattern of the as-synthesized Zn sample (Figure 1 B), with the intensity of the oxide peaks being notably higher compared to B-Cu due to faster oxidation of metallic Zn.

The transmission electron microscopy (TEM) image (Figure 1 C) reveals the nanoparticle morphology of the as-synthesized B-Cu sample with some degree of agglomeration. The corresponding size distribution histogram (Figure S1) shows that the B-Cu nanoparticle sizes were in the 23–31 nm range. The as-synthesized Zn sample (Figure 1 D) exhibits nanosheet morphology. High-resolution transmission electron microscopy (HRTEM) images of the B-Cu sample (Figure 1 E) show lattice fringes with three different d-spacings of 3.01, 2.46, and 2.13 Å, which correspond to Cu$_2$O (110), (111), and (200), respectively, while no metallic Cu-related lattice fringes were observed. This is most likely due to the surface oxide-covered metallic Cu phase making it difficult to be observed by HRTEM. Similarly, only ZnO (100) and (101) lattice fringes with d-spacings of 2.81 and 2.47 Å, respectively, were identified in Zn nanosheets (Figure 1 F).

X-ray photoelectron spectroscopy (XPS) was employed in order to study the chemical states and composition of the catalysts. The XP spectrum of B-Cu nanoparticles presents a sharp Cu 2p$_{3/2}$ peak at 932.4 eV (Figure S2), which can be

assigned to Cu^0 and/or Cu^+ species.[30] To distinguish Cu^0 and Cu^+, the Cu LMM Auger transition (Figure 2 A) was additionally recorded, which indicates that the surface of B-Cu nanoparticles mainly consisted of a Cu^+ (Cu_2O) oxidation state at a kinetic energy of 916.7 eV. This result is consistent with the HRTEM analysis. The presence of B in B-Cu was confirmed by B 1s XPS. Only B sub-oxide signals at about 191.0 eV were observed in the B 1s spectrum (Figure 2 B), since the solubility of B in Cu is extremely low and elemental B is typically oxidized at the surface. The B:Cu atom ratio in the B-doped Cu sample is 0.0144 as determined by XPS. Figure 2 C presents the Zn 2p XP spectrum of Zn nanosheets with a sharp $Zn 2p_{3/2}$ peak at 1022 eV. Zn^0 and Zn^{2+} (ZnO) can be distinguished using the Zn LMM spectrum (Figure 2 D), in which the well-resolved peak at around 987.8 eV is assigned to ZnO. ZnO as the main component on the surface of Zn nanosheets matches well with the HRTEM analysis in Figure 1 F.

The electrocatalytic activity and selectivity of the catalysts towards eCO_2RR were evaluated in a H-type GDE cell (Figure S3) employing 1 M aqueous KOH as electrolyte. In our experiments, the catalyst ink was directly drop-coated on carbon paper with a hydrophobic microporous gas diffusion layer (GDL) to obtain the GDE (see details in Supporting Information). GDEs having only B-Cu in the catalyst layer show that the predominant product during eCO_2RR is H_2 over the whole applied current range (Figure S4A). The Faradaic efficiency (FE) for H_2 was 78%, the FE for C_1 products (CO and formate) was 4.8%, and the FE for C_2 products (C_2H_4 and C_2H_5OH) was 5.8%, at a current density of -200 mA cm^{-2} and a potential of -0.6 V vs. RHE (Figure 3 A, Figure S4A). The comparatively high FE for H_2 evolution can be ascribed to the high hydrophilicity of the B-Cu catalyst as demonstrated by contact angle measurements (Figure S5). Moreover, the hydrophilic property of B-Cu accelerates flooding of the GDE, thus limiting eCO_2RR.
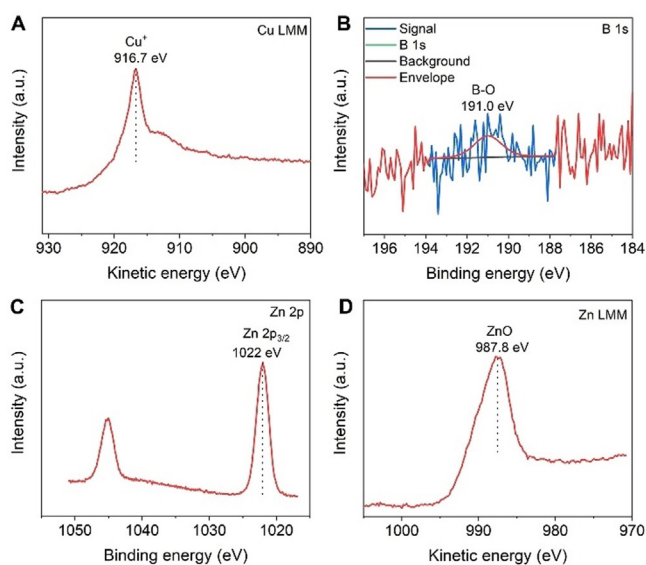
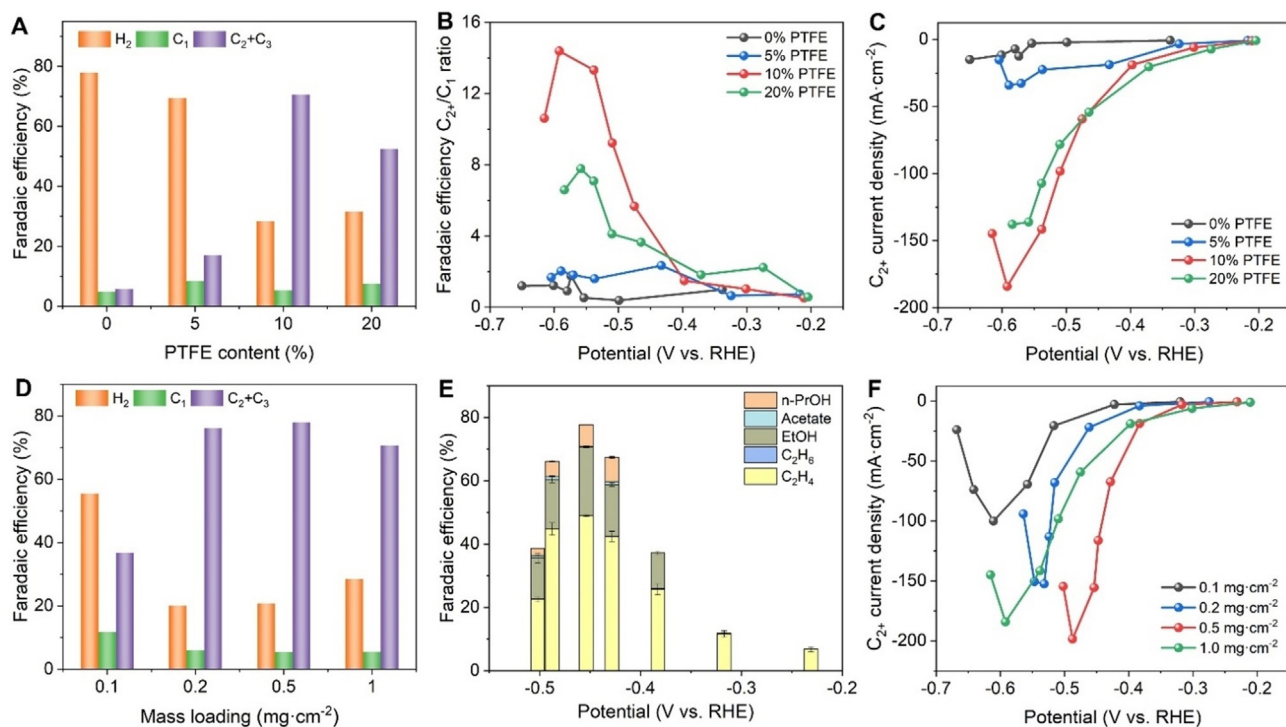At a current density of -400 mA cm^{-2}, H_2 is the only detectable product, and the electrolyte penetrated the whole GDE as leakage was observed.

To mitigate the flooding problem, we added varying amounts of PTFE to the catalyst ink to enhance the hydrophobicity of the B-Cu catalyst layer on top of the GDE. By increasing the content of PTFE relative to the total mass loading of the catalyst from 5 to 10 and 20%, the hydrophobicity of the B-Cu GDE gradually increased as shown in the corresponding contact angle measurements (Figure S5). As expected, the hydrogen evolution reaction (HER) was substantially decreased and the formation of C_{2+} products, mainly ethylene and ethanol, was enhanced accordingly (Figure S4). For B-Cu-modified GDEs with 5% PTFE, the FE for H_2 decreased to 69% at a current density of -200 mA cm^{-2} and a potential of -0.59 V vs. RHE, the FE for C_1 products increased to 8.4% (CO 3.1%, formate 4.4%), and the FE for C_{2+} products increased to 17% (C_2H_4 5%, C_2H_5OH 12%; Figure 3 A, Figure S4B). When the content of PTFE was further increased to 10%, the FE for H_2 was further reduced to 28% at a current density of -200 mA cm^{-2} and a potential of -0.54 V vs. RHE, at which the FE for C_1 products decreased to 5% (CO 4%, formate 1.0%), and the FE for C_{2+} products increased to 70% (C_2H_4 43%, C_2H_5OH 23%, C_3H_7OH 4%; Figure 3 A, Figure S4C). However, further increase in the PTFE content to 20% did not lead to a decrease in the HER (32% at -200 mA cm^{-2}, -0.54 V vs. RHE). Concomitantly, the FE for C_1 products increased to 8% (CO 6%, formate 2%), and the FE for C_{2+} products decreased to 53% (C_2H_4 27%, C_2H_5OH 20%, C_3H_7OH 5%; Figure 3 A, Figure S4D). This is most likely due to a decrease in conductivity of the B-Cu catalyst/PTFE layer and possible blocking of the active sites of the catalyst. B-Cu GDEs with 10% PTFE exhibited the maximum FE for the formation of C_{2+} products and the minimum FE for H_2 and C_1 products formation.

The selectivity of eCO_2RR to C_{2+} products on B-Cu GDEs with different contents of PTFE can be further evaluated by the FE for the C_{2+}/C_1 products ratio. As shown in Figure 3 B, B-Cu-10%PTFE is highly selective for the formation of C_{2+} products at potentials more negative than -0.43 V vs. RHE. Particularly, at -0.59 V vs. RHE and -300 mA cm^{-2}, the C_{2+}/C_1 ratio of B-Cu-10%PTFE reaches 14.4, which is superior to electrodes with 0, 5, and 20% PTFE. The selectivity of eCO_2RR to C_{2+} products on B-Cu-10%PTFE GDEs reached up to 93.5% (Figure S8).

The overpotential for eCO_2RR at a total current density of -10 mA cm^{-2} decreases with increasing PTFE added to the B-Cu GDE (Figure S9). The total current density, as well as the partial current densities for C_{2+} product formation were greatly enhanced upon the addition of PTFE on the B-Cu GDE (Figure 3 C). B-Cu-10%PTFE shows the maximum C_{2+} geometric current density of -184 mA cm^{-2} at -0.59 V vs. RHE, which is around 16 times higher than that obtained using B-Cu without PTFE (-11.6 mA cm^{-2}). We conclude that the intermediate amount of PTFE (10%) can balance hydrophobicity and conductivity of B-Cu and mitigate the flooding problem of the GDE, thereby boosting the conversion of CO_2 towards C_{2+} compounds.

Figure 2. A) Cu LMM and B) B 1s XPS spectra for B-Cu nanoparticles. C) Zn 2p and D) Zn LMM spectra for Zn nanosheets.

Figure 3. A) FE of H_2, C_1, and C_{2+} products on B-Cu electrodes with 0, 5, 10, and 20% PTFE at a current density of -200 mA cm^{-2} and a potential of -0.60, -0.59, -0.54, and -0.54 V vs. RHE, respectively. B) C_{2+}/C_1 ratio and C) partial current density of C_{2+} products at different potentials on B-Cu electrodes with different contents of PTFE. D) FE for the formation of H_2, C_1, and C_{2+} products on B-Cu electrodes with 0.1, 0.2, 0.5, and 1.0 mg cm^{-2} at a current density of -200 mA cm^{-2} and a potential of -0.64, -0.53, -0.45, and -0.54 V vs. RHE, respectively. E) FE for the formation of various C_{2+} products at a catalyst loading of 0.5 mg cm^{-2} B-Cu at different potentials. F) Partial current density of C_{2+} products at different potentials on B-Cu electrodes with different loadings. Product quantification was performed by means of gas chromatography (Figure S6) and ^{1}H-NMR spectroscopy (Figure S7).

The three-phase interphase within the GDE plays a key role for the eCO$_2$RR, which can be affected by the thickness of the catalyst layer. Hence, we further changed the mass loading of the catalyst to investigate the effect of catalyst thickness on the eCO$_2$RR at the three-phase interphase. The thickness of the catalyst layer on the top of GDL gradually decreases from 26.7 μm to 13.4, 5.5 and 2.5 μm when decreasing the mass loading of the catalyst from 1 mg cm^{-2} to 0.5, 0.2 and 0.1 mg cm^{-2}, respectively (Figure S10). With decreasing mass loading of B-Cu, the FE for H$_2$ formation was further decreased to about 20% with a catalyst loading of 0.5 and 0.2 mg cm^{-2}, respectively, at -200 mA cm^{-2}, while it increased to 56% when only 0.1 mg cm^{-2} of the catalyst was used (Figure S11). In the case of a too thin catalyst layer, the electrolyte will penetrate into the GDL causing flooding which is ultimately promoting the HER and inhibiting the eCO$_2$RR. For example, on B-Cu GDEs with a mass loading of only 0.1 mg cm^{-2}, H$_2$ formation accounted for 85% of the current at -300 mA cm^{-2}. Further increase of the current density to -400 mA cm^{-2} led to increasing electrowetting and hence penetration of the electrolyte through the GDE, ultimately causing the GDE to lose its function.
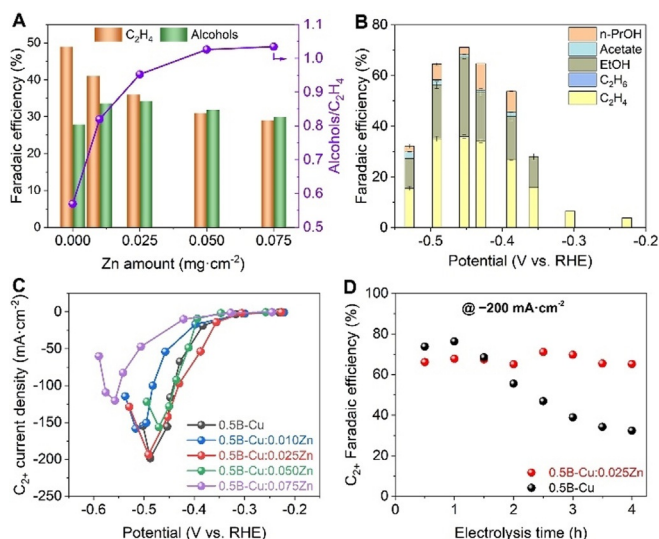
The formation of CH$_4$ was completely suppressed at a loading of 1.0 mg cm^{-2}, however, decreasing the loading to 0.5 mg cm^{-2} led to CH$_4$ formation with a FE of around 0.02% at -200 mA cm^{-2}. The FE for CH$_4$ formation gradually

increased to 0.5 and 8% at loadings of 0.2 and 0.1 mg cm^{-2}, respectively (Figure S11, S12), suggesting that the formation of C$_1$ products increases with decreasing catalyst loading (Figure 3D). Typically, at -200 mA cm^{-2}, the FE for C$_2$H$_4$ first increased to 49% for loadings of 0.5 and 0.2 mg cm^{-2}, and then decreased to 18% for a loading of 0.1 mg cm^{-2}, whereas the FE for C$_2$H$_5$OH gradually decreased to 22 and 18% for loadings of 0.5 and 0.2 mg cm^{-2}, and further decreased at 14% for a loading of 0.1 mg cm^{-2} (Figure S11). In summary, the FE for C$_{2+}$ compounds including C$_2$H$_4$, C$_2$H$_5$OH, C$_3$H$_7$OH, and acetate was 78% for a loading of 0.5 mg cm^{-2} (Figure 3D), consisting of 49% C$_2$H$_4$, 22% C$_2$H$_5$OH, 7% C$_3$H$_7$OH at a current density of -200 mA cm^{-2} and a potential of -0.45 V vs. RHE (Figure 3E).

The current density at potentials more negative than -0.40 V vs. RHE first increases by decreasing the catalyst loading from 1 to 0.5 mg cm^{-2} and then decreases with further lowering the mass loadings to 0.2 and 0.1 mg cm^{-2} (Figure S13), which coincides with the partial current for the eCO$_2$RR. This can be further confirmed by a comparison of the partial current densities for C$_{2+}$ formation as shown in Figure 3F. The highest C$_{2+}$ current density of -198 mA cm^{-2} (at -0.49 V vs. RHE) was achieved at a loading of 0.5 mg cm^{-2} of B-Cu GDE. In contrast, the maximum C$_{2+}$ current density for catalyst loadings of 1.0, 0.2, and 0.1 mg cm^{-2}, was 184, 152, and 69 mA cm^{-2} at more negative potentials of -0.59, -0.53,

and −0.56 V vs. RHE, respectively. This implies that the mass loading of the B-Cu catalyst, and thus the thickness of the catalyst layer, considerably influences the location of the three-phase interphase and the contribution of eCO$_2$RR to the overall current. A suitable penetration depth of the electrolyte on the one hand together with a sufficient diffusion depth of gaseous CO$_2$ on the other hand are necessary to maximize the activity and efficiency of eCO$_2$RR.

To address the cathodic corrosion issue of Cu catalysts at high cathodic potentials, which limits the long-term stability of such catalysts, the less noble metal Zn was employed as sacrificial anode to protect the B-Cu catalyst. For this, a B-Cu-Zn catalyst was prepared by physical mixing of B-Cu nanoparticles and Zn nanosheets on a carbon paper as support. The B-Cu loading was fixed at 0.5 mg cm^{-2} while the Zn loading was increased gradually from 0.01 to 0.075 mg cm^{-2}. The maximum FEs for the formed C$_2$H$_4$, C$_2$H$_5$OH and C$_3$H$_7$OH and their corresponding potentials can both be adjusted by varying the Zn loading in the B-Cu-Zn catalyst (Figure S14). The catalyst with a composition of 0.5 B-Cu:0.025 Zn showed the highest FE for alcohols (34 %), with C$_2$H$_5$OH (31 %) and C$_3$H$_7$OH (3 %) at −0.45 V vs. RHE and a total current density of −200 mA cm^{-2} (Figure 4 A,B). Further increasing the Zn loading results in a decline of the maximum FE for the formation of C$_2$H$_5$OH, which can be attributed to the excess CO generated on Zn (Figure S15) and the competing HER. The maximum FE for the formation of C$_2$H$_4$ monotonically decreases from 49 % on B-Cu to 27 % on 0.5 B-Cu:0.075 Zn. Hence, the selectivity for alcohols versus C$_2$H$_4$ (FE alcohols / FE C$_2$H$_4$) can be tuned from 0.57 on a bare B-Cu electrode to 1.04 on a 0.5 B-Cu:0.075 Zn electrode by the amount of added Zn nanosheets (Figure 4 A).
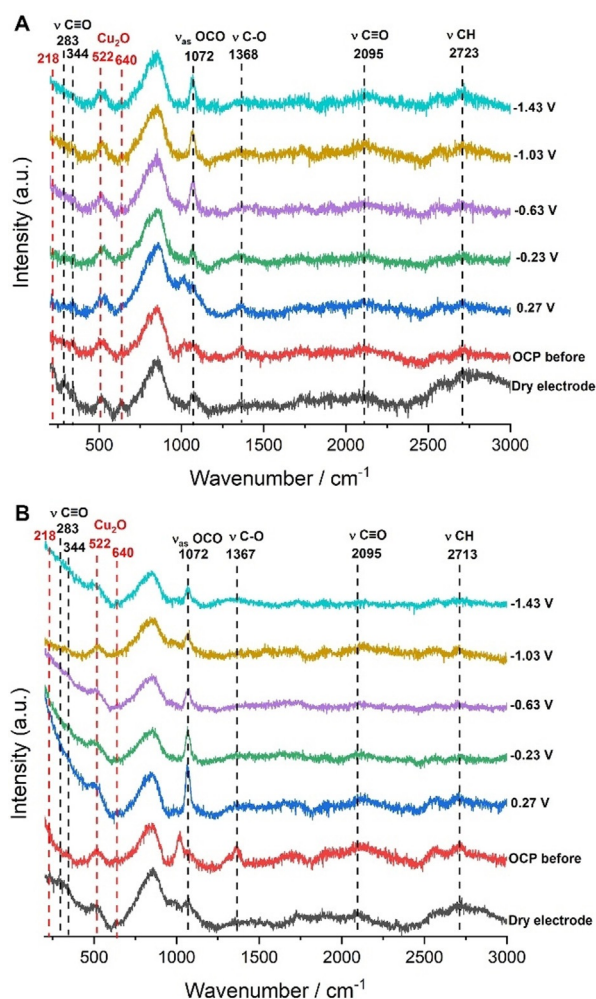
The current density at potentials more positive than −0.45 V vs. RHE was highest using a 0.5 B-Cu:0.025 Zn GDE, while at potentials more negative than −0.45 V vs. RHE, the current density was highest at a higher Zn loading of 0.5 B-Cu:0.05 Zn GDE (Figure S16). Further increasing the Zn loading to 0.075 mg cm^{-2} resulted in a drop of current density due to the excess of Zn and fewer Cu active sites for eCO$_2$RR. The partial current densities for the formation of C$_{2+}$ products are further compared in Figure 4 C. Using a 0.5 B-Cu:0.025 Zn GDE, the highest current density for the formation of C$_{2+}$ products is obtained over almost the whole potential range, with an observed value of −194 mA cm^{-2} at −0.49 V vs. RHE being similar to that of the B-Cu electrode. In contrast, using GDEs with catalyst loadings of 0.5 mg cm^{-2} B-Cu GDEs mixed with 0.01, 0.05, and 0.075 mg cm^{-2} Zn nanosheets, maximum C$_{2+}$ product formation current densities of −158, −156, and −120 mA cm^{-2} were obtained at potentials of −0.52, −0.47, and −0.56 V vs. RHE, respectively. Hence, an optimum amount of Zn (0.025 mg cm^{-2}) is required for minimizing cathodic Cu corrosion while retaining reasonable activity of C$_{2+}$ product formation.

The long-term eCO$_2$RR stability of the catalyst is one of the key factors for potential applications, notwithstanding the fact that maintaining the catalyst integrity still remains challenging for GDE-based systems. The stability of the 0.5 B-Cu:0.025 Zn electrode in comparison with a B-Cu electrode was evaluated by performing eCO$_2$RR electrolysis at a high current density of −200 mA cm^{-2}. The experimental results shown in Figure 4 D and Figure S17 reveal excellent stability of the 0.5 B-Cu:0.025 Zn electrode with a negligible decay of the FE for the formation of C$_{2+}$ products. In contrast, the FE for the formation of C$_{2+}$ products on B-Cu GDEs starts to attenuate after 1 h of eCO$_2$RR electrolysis at the expense of increasing H$_2$ formation. Thus, the incorporation of Zn nanosheets remarkably improved the long-term eCO$_2$RR stability of the catalyst, however with sacrificing a little bit of the FE for the formation of C$_{2+}$ products at the beginning of the electrolysis. To better understand the difference in the observed long-term stability of these two kinds of GDEs, the change in composition and chemical states after electrocatalysis was further investigated by recording Cu and Zn LMM Auger spectra before and after the stability test. Qualitative assessment of the Cu LMM Auger spectra (Figure S18) reveals Cu$^+$ with a peak maximum at around 916.3 eV kinetic energy to be the main surface component in both the 0.5B-Cu:0.025Zn GDE and the B-Cu GDE even after long-term eCO$_2$RR. Besides Cu$^+$, a contribution of metallic Cu manifests as a shoulder at a kinetic energy of around 918.5 eV. Interestingly, that contribution diminishes nearly completely after 4 h of electrolysis for the B-Cu GDE, whereas the 0.5B-Cu:0.025Zn GDE retains a visible shoulder corresponding to Cu^0 after the same duration of electrolysis. These findings demonstrate the stabilization of the metallic Cu state on the GDE surface by Zn in 0.5B-Cu:0.025Zn. Further evidence for the sacrificial anodic protection effect of Zn is obtained from the Zn LMM Auger spectra on 0.5B-Cu:0.025Zn GDE before and after 15 min of eCO$_2$RR (Figure S19). While the as-prepared GDE shows similar contributions of metallic Zn and ZnO, the GDE after 15 min

Figure 4. A) FE for the formation of C$_2$H$_4$ and alcohols and the ratios of alcohols/C$_2$H$_4$ on B-Cu electrodes with different amounts of Zn at a current density of −200 mA cm^{-2}. B) FE for the formation of various C$_{2+}$ products on 0.5 B-Cu:0.025 Zn electrodes at different potentials. C) Partial current density for the formation of C$_{2+}$ products at different potentials on B-Cu electrodes with different amounts of Zn. D) FE for the formation of various C$_{2+}$ products on 0.5 B-Cu and 0.5 B-Cu:0.025 Zn GDEs at a current density of −200 mA cm^{-2} and 4 h of electrolysis.

of eCO$_2$RR exhibits a stronger decay of the Zn^0 peak intensity compared to the one of ZnO. Notably, no traces of surface Zn are detectable after 4 h of electrolysis (spectrum not shown) confirming the anodic Zn corrosion process concomitantly stabilizing Cu$^+$ and Cu^0. This finding does not only explain the higher stability of the 0.5 B-Cu:0.025 Zn GDE, but also confirms the synergistic function of the presence of Cu$^+$ and Cu^0 to promote C$_{2+}$ product formation. The obtained Cu LMM Auger spectra (Figure S18) confirmed that both the 0.5 B-Cu:0.025 Zn GDE and the B-Cu GDE mainly exhibit Cu$^+$ on the surface even after long-term eCO$_2$RR. Besides Cu$^+$, a fraction of Cu^0 was also observed which marginally increased during electrolysis. The 0.5 B-Cu:0.025 Zn GDE shows a more stable Cu$^+$/Cu^0 ratio after 4 h of electrolysis with a lower Cu$^+$/Cu^0 ratio due to the Zn protection as compared with the 0.5 B-Cu GDE. This finding does not only explain the higher stability of the 0.5 B-Cu:0.025 Zn GDE, but also confirms the synergistic function of the presence of Cu$^+$ and Cu^0 to promote C$_{2+}$ product formation. The obtained Zn LMM Auger spectra on 0.5 B-Cu:0.025 Zn GDE (Figure S19) shows a significant decrease

of both Zn content and metallic Zn after long-term eCO$_2$RR, which confirms the sacrificial protection effect of Zn on the B-Cu catalyst.

To further investigate the origin of the eCO$_2$RR performance of both the B-Cu and 0.5 B-Cu:0.025 Zn GDEs, operando Raman spectroscopy measurements were carried out by sequential application of potentials from 0.27 to −1.43 V vs. RHE. First, the structural evolution of the catalyst was monitored (Figure 5). Both 0.5 B-Cu and 0.5 B-Cu:0.025 Zn GDEs exhibit Raman peaks at 218, 522, and 640 cm^{-1}, which were ascribed to the Cu$_2$O phase.[18,31,32] These Raman signals remain essentially unchanged under operando conditions demonstrating the stability of the active Cu$^+$ species even at high reduction potentials. This is expected to contribute to the efficient conversion of CO$_2$ to C$_{2+}$ products at the comparatively high applied current densities. Operando electrochemistry Raman measurements were additionally used to detect possible intermediates of the eCO$_2$RR on 0.5 B-Cu and 0.5 B-Cu:0.025 Zn electrodes. The peak at 1072 cm^{-1} is assigned to the anti-symmetrical stretching of *OCO,[32,33] which can be observed from a potential of below −0.23 V vs. RHE and increases in intensity at more cathodic potentials for the 0.5 B-Cu electrode (Figure 5 A). In contrast, the 0.5 B-Cu:0.025 Zn electrode already shows a sharp *OCO vibrational peak at a potential of 0.27 V vs. RHE, which gradually weakens at more cathodic potentials (Figure 5 B). This implies that the activation of CO$_2$ can be achieved at more positive potentials for the 0.5 B-Cu:0.025 Zn electrode additionally supporting the observed higher eCO$_2$RR activity for the 0.5 B-Cu:0.025 Zn electrode as compared with the 0.5 B-Cu electrode (Figure 4 C). Raman peaks at 283, 344, and 2095 cm^{-1} for both 0.5 B-Cu and 0.5 B-Cu:0.025 Zn electrodes correspond to adsorbed CO on Cu,[31–34] which represents the key intermediate for C−C coupling and C$_{2+}$ products formation. The peak at about 2713 cm^{-1} is associated to the C−H vibration[35] and further confirms the formation of hydrocarbons.

Conclusion

A B-Cu GDE system was developed for selective CO$_2$ conversion to C$_{2+}$ products at seldom reported high current densities. The flooding problem in this GDE system, that is, liquid electrolyte domination at the triple-phase boundary, was mitigated through controlling the amount of added PTFE and by optimizing the catalyst loading leading to optimisation of the gas-liquid-catalyst interphase. The FE for the formation of C$_{2+}$ products was as high as 78 % on a 0.5 mg cm^{-2} B-Cu GDE with 10 % PTFE at a current density of −200 mA cm^{-2} and a potential of −0.45 V vs. RHE. By incorporation of an optimum amount of Zn nanosheets (0.025 mg cm^{-2}), the activity and long-term stability of the B-Cu catalyst were substantially improved reaching a maximum current density for the formation of C$_{2+}$ products of −194 mA cm^{-2}. Operando electrochemical Raman results demonstrate the stable presence of Cu$^+$ species during eCO$_2$RR and the positive shift of the overpotential for *OCO formation upon incorporation of Zn, which concertedly result in the excellent eCO$_2$RR

Figure 5. Operando electrochemistry Raman spectra for a A) 0.5 B-Cu GDE and a B) 0.5 B-Cu:0.025 Zn GDE during eCO$_2$RR at different applied potentials.

performance of the B-Cu-Zn GDE. These findings suggest a strategy for optimizing GDE structures to ultimately improve the eCO₂RR activity, selectivity, and stability for the formation of value-added chemicals/fuels at high current densities which may become suitable for potential applications.

Conflict of interest

The authors declare no conflict of interest.

[1] P. Tans, R. Keeling, NORR/ESRL. http://www.esrl.noaa.gov/gmd/ccgg/trends/.

[2] W. D. Jones, *J. Am. Chem. Soc.* **2020**, *142*, 4955–4957.

[3] C. Chen, J. F. K. Kotyk, S. W. Sheehan, *Chem* **2018**, *4*, 2571–2586.

[4] Y. Y. Birdja, E. Perez-Gallent, M. C. Figueiredo, A. J. Göttle, F. Calle-Vallejo, M. T. M. Koper, *Nat. Energy* **2019**, *4*, 732–745.

[5] M. B. Ross, P. D. Luna, Y. Li, C. T. Dinh, D. Kim, P. Yang, E. H. Sargent, *Nat. Catal.* **2019**, *2*, 648–658.

[6] S. Zhang, Q. F. Rong, T. J. Meyer, *Chem* **2018**, *4*, 2571–2586.

[7] T. Burdyny, W. A. Smith, *Energy Environ. Sci.* **2019**, *12*, 1442–1453.

[8] M. Ma, E. L. Clark, K. T. Therkildsen, S. Dalsgaard, I. Chorkendorff, B. Seger, *Energy Environ. Sci.* **2020**, *13*, 977–985.

[9] F. P. García de Arquer, C. T. Dinh, A. Ozden, J. Wicks, C. McCallum, A. R. Kirmani, D. H. Nam, C. Gabardo, A. Seifitokaldani, X. Wang, Y. C. Li, F. Li, J. Edwards, L. J. Richter, S. J. Thorpe, D. Sinton, E. H. Sargent, *Science* **2020**, *367*, 661–666.

[10] A. Vasileff, C. Xu, Y. Jiao, Y. Zheng, S. Z. Qiao, *Chem* **2018**, *4*, 1809–1831.

[11] C. W. Lee, K. D. Yang, D. H. Nam, J. H. Jang, N. H. Cho, S. W. Im, K. T. Nam, *Adv. Mater.* **2018**, *30*, 1704717.

[12] C. W. Li, M. W. Kanan, *J. Am. Chem. Soc.* **2012**, *134*, 7231–7234.

[13] D. Ren, Y. Deng, A. D. Handoko, C. S. Chen, S. Malkhandi, B. S. Yeo, *ACS Catal.* **2015**, *5*, 2814–2821.

[14] Q. Zhu, X. Sun, D. Yang, J. Ma, X. Kang, L. Zheng, J. Zhang, Z. Wu, B. Han, *Nat. Commun.* **2019**, *10*, 3851.

[15] A. Eilert, F. Cavalca, F. S. Roberts, J. Osterwalder, C. Liu, M. Favaro, E. J. Crumlin, H. Ogasawara, D. Friebel, L. G. M. Pettersson, A. Nilsson, *J. Phys. Chem. Lett.* **2017**, *8*, 285–290.

[16] H. Mistry, A. S. Varela, C. S. Bonifacio, I. Zegkinoglou, I. Sinev, Y. W. Choi, K. Kisslinger, E. A. Stach, J. C. Yang, P. Strasser, B. Roldan Cuenya, *Nat. Commun.* **2016**, *7*, 12123.

[17] P. De Luna, R. Quintero-Bermudez, C. T. Dinh, M. B. Ross, O. S. Bushuyev, P. Todorović, T. Regier, S. O. Kelley, E. H. Sargent, *Nat. Catal.* **2018**, *1*, 103–110.

[18] P. P. Yang, X. L. Zhang, F. Y. Gao, Y. R. Zheng, Z. Z. Niu, X. Yu, R. Liu, Z. Z. Wu, S. Qin, L. P. Chi, Y. Duan, T. Ma, X. S. Zheng, J. F. Zhu, H. J. Wang, M. R. Gao, S. H. Yu, *J. Am. Chem. Soc.* **2020**, *142*, 6400–6408.

[19] Z. Yin, C. Yu, Z. Zhao, X. Guo, M. Shen, N. Li, M. Muzzio, J. Li, H. Liu, H. Lin, J. Yin, G. Lu, D. Su, S. Sun, *Nano Lett.* **2019**, *19*, 8658–8663.

[20] Z. Q. Liang, T. T. Zhuang, A. Seifitokaldani, J. Li, C. W. Huang, C. S. Tan, Y. Li, P. De Luna, C. T. Dinh, Y. Hu, Q. Xiao, P. L. Hsieh, Y. Wang, F. Li, R. Quintero-Bermudez, Y. Zhou, P. Chen, Y. Pang, S. C. Lo, L. J. Chen, H. Tan, Z. Xu, S. Zhao, D. Sinton, E. H. Sargent, *Nat. Commun.* **2018**, *9*, 3828.

[21] C. Chen, X. Sun, L. Lu, D. Yang, J. Ma, Q. Zhu, Q. Qian, B. Han, *Green Chem.* **2018**, *20*, 4579–4583.

[22] Y. Zhou, F. Che, M. Liu, C. Zou, Z. Liang, P. De Luna, H. Yuan, J. Li, Z. Wang, H. Xie, H. Li, P. Chen, E. Bladt, R. Quintero-Bermudez, T. K. Sham, S. Bals, J. Hofkens, D. Sinton, G. Chen, E. H. Sargent, *Nat. Chem.* **2018**, *10*, 974–980.

[23] S. Popović, M. Smiljanić, P. Jovanovič, J. Vavrac, R. Buonsanti, N. Hodnik, *Angew. Chem. Int. Ed.* **2020**, *59*, 14736–14746; *Angew. Chem.* **2020**, *132*, 14844–14854.

[24] L. Fan, C. Xia, F. Yang, J. Wang, H. Wang, Y. Lu, *Sci. Adv.* **2020**, *6*, eaay3111.

[25] C. T. Dinh, T. Burdyny, M. G. Kibria, A. Seifitokaldani, C. M. Gabardo, F. P. G. de Arquer, A. Kiani, J. P. Edwards, P. De Luna, O. S. Bushuyev, C. Zou, R. Quintero-Bermudez, Y. Pang, D. Sinton, E. H. Sargent, *Science* **2018**, *360*, 783–787.

[26] A. I. Yanson, P. Rodriguez, N. Garcia-Araez, R. V. Mom, F. D. Tichelaar, M. T. M. Koper, *Angew. Chem. Int. Ed.* **2011**, *50*, 6346–6350; *Angew. Chem.* **2011**, *123*, 6470–6474.

[27] B. Vanrenterghem, M. Bele, F. R. Zepeda, M. Šala, N. Hodnik, T. Breugelmans, *Appl. Catal. B* **2018**, *226*, 396–402.

[28] S. Ma, M. Sadakiyo, M. Heima, R. Luo, R. T. Haasch, J. I. Gold, M. Yamauchi, P. J. Kenis, *J. Am. Chem. Soc.* **2017**, *139*, 47–50.

[29] Y. X. Duan, F. L. Meng, K. H. Liu, S. S. Yi, S. J. Li, J. M. Yan, Q. Jiang, *Adv. Mater.* **2018**, *30*, 7873–7889.

[30] H. Jung, S. Y. Lee, C. W. Lee, M. K. Cho, D. H. Won, C. Kim, H. S. Oh, B. K. Min, Y. J. Hwang, *J. Am. Chem. Soc.* **2019**, *141*, 4624–4633.

[31] Y. Deng, B. S. Yeo, *ACS Catal.* **2017**, *7*, 7873–7889.

[32] Y. Yang, S. Ajmal, Y. Feng, K. Li, X. Zheng, L. Zhang, *Chem. Eur. J.* **2020**, *26*, 4080–4089.

[33] W. Shan, R. Liu, H. Zhao, Z. He, Y. Lai, S. Li, G. He, J. Liu, *ACS Nano* **2020**, *14*, 11363–11372.

[34] D. Ren, B. S.-H. Ang, B. S. Yeo, *ACS Catal.* **2016**, *6*, 8239–8247.

[35] D. Öhl, Y. U. Kayran, J. R. C. Junqueira, V. Eßmann, T. Bobrowski, W. Schuhmann, *Langmuir* **2018**, *34*, 12293–12301.